Journal of Alloys and Compounds 772 (2019) 186–192

Contents lists available at ScienceDirect

Journal of Alloys and Compounds

journal homepage: http://www.elsevier.com/locate/jalcom

Preparation and hydrogen storage of Pd/MIL-101 nanocomposites

Yanliang Zhao [a, b], Fei Liu [a, b, *], Junhua Tan [a], Peng Li [a, **], Zhongmin Wang [c, ***], Kaijin Zhu [a], Xianmin Mai [g, ****], Hu Liu [d, e], Xiaojing Wang [d, f], Yong Ma [i, *****], Zhanhu Guo [d, ******]

[a] Department of Materials Engineering, Taiyuan Institute of Technology, Taiyuan, 030008, China
[b] School of Material Science and Engineering, North University of China, Taiyuan, 030008, China
[c] School of Material Science and Engineering, Guilin University of Electronic Technology, Guilin, 541004, China
[d] Integrated Composites Laboratory (ICL), Department of Chemical & Biomolecular Engineering, University of Tennessee, Knoxville, TN, 37996, USA
[e] National Engineering Research Center for Advanced Polymer Processing Technology, Zhengzhou University, Zhengzhou, 450002, China
[f] School of Material Science and Engineering, Jiangsu University of Science and Technology, Zhenjiang, Jiangsu, 212003, China
[g] School of Urban Planning and Architecture, Southwest Minzu University, Chengdu, 610041, China
[i] College of Materials Science and Engineering, Shandong University of Science and Technology, Qingdao, 266590, China

ARTICLE INFO

Article history:
Received 4 August 2018
Received in revised form
1 September 2018
Accepted 4 September 2018
Available online 5 September 2018

Keywords:
MIL-101
Pd/MIL-101
Hydrogen storage
Hydrogen-diffusion coefficient (DH)

ABSTRACT

The structures and hydrogen adsorption properties of $\{Cr_3F(H_2O)_2O[(O_2C)\text{-}C_6H_4\text{-}(CO_2)]_3 \cdot nH_2O(n\sim25)\}$ (MIL-101) and its Pd composites have been investigated by X-ray diffraction (XRD) analysis, transmission electron microscope (TEM), X-ray photoelectron spectroscopy (XPS), and specific surface area tests (BET). The as-prepared Pd/MIL-101 composites were microporous and maintained three-dimensional topology of MIL-101 before and after Pd loading that existed in the skeleton. A carbon bridge was formed between Pd metal and MIL-101 to improve the hydrogen storage. The loaded Pd reduced the hydrogen absorption enthalpy of MIL-101, and thus improved the storage of hydrogen compared with MIL-101. The diffusion coefficient reached 7.233×10^{-9} in the Pd/MIL-101 nanocomposites.

1. Introduction

Nowadays, clean hydrogen without producing pollution after combustion becomes an alternative to traditional fossil resources. People hope to use this hydrogen energy to solve the problem of fossil energy depletion and environmental pollution. Safe and efficient H_2 storage technology and H_2 storage materials are common challenges and are important for improving the hydrogen storage capacity and stability of hydrogen storage materials further [1,2].

Metal organic frameworks (MOFs), a kind of organic-inorganic hybrid porous zeolite material, belong to a new type of material. Its basic structure is a multi dimensional infinite structure in space, and is composed of multi tooth organic ligands and transition metal ions through coordination bonds. It possesses special properties such as high specific surface area (up to 4000 m^2/g), high crystallinity, and high porosity (up to 90%). MIL-101 is one of the most typical carriers and it has a large specific surface area (up to 5900 m^2/g), large pore volume (up to 702 nm^3) and pore size (up to 2.9–3.4 nm) [2]. Compared with other existing materials, such as metal, ceramic and polymer composite systems [3–5], MOFs have shown broad prospects in gas storage, especially hydrogen storage, and have become a hot topic in the field of hydrogen carrier materials. MOFs have attracted wide attention in the fields of luminescence, catalysis and adsorption because of their higher porosity and specific surface area, light skeleton density, good crystallinity, and chemical regulation of their structures. It is a particularly active subject in the field of materials [6–8]. For example, Yaghi et al. reported a MOF-$Zn_4O(BDC)_3$ in 2003. The hydrogen storage capacity of the material at −195.2 °C and medium pressure was high.

* Corresponding author.Department of Materials Engineering, Taiyuan Institute of Technology, Taiyuan, 030008, China.
** Corresponding author.
*** Corresponding author.
**** Corresponding author.
***** Corresponding author.
****** Corresponding author.
E-mail addresses: zhaoyanliang8205@163.com (Y. Zhao), houmaliufei999@163.com (F. Liu), zmwang@guet.edu.cn (Z. Wang), maixianmin@foxmail.com (X. Mai), mayongfn@gmail.com (Y. Ma), zguo10@utk.edu (Z. Guo).

https://doi.org/10.1016/j.jallcom.2018.09.045
0925-8388/

The storage density of hydrogen was 4.5 wt% [9]. The hydrogen absorption of MOF-5 under the condition of 298 K and 2 MPa was 1.0 wt.%, the capacity of this MOF series with changing organic links was almost the same. The hydrogen storage properties of porous polymers with topological structures had been improved obviously. IRMOF-13 had the highest hydrogen storage capacity, two times of that of MOF-5 [10,11]. The pore size of MOF-177 was 1.09–1.18 nm, which was the largest known MOF compound [12].

However, MOFs are mainly physical adsorption. There are some solvent molecules in the MOF frame. It is difficult to remove all the solvent molecules in the skeleton only by heating up with the premise of keeping the skeleton in good condition. The greatest advantage of MOFs is that the size of the pore size can be adjusted by changing organic ligands to regulate the specific surface area of porous ligand polymer and to increases the storage space, thus improving the adsorption of hydrogen molecules. For example, Mulfort et al. modified the MOFs of mixed ligands and oxidized lithium. Lithium ion and bond with the skeleton significantly increased the hydrogen storage capacity of the complex at liquid nitrogen temperature [13]. Sun et al. doped noble metal/activated carbon to MOFs, and the amount of hydrogen storage was increased from 0.37 wt.% to 1.14 wt.% at room temperature [14]. Meanwhile, the heteroatom nickel has strengthened the iron plate by surface mechanical attrition alloy and heat treatment [15].

MOFs play a key role in the field of hydrogen storage. $\{Cr_3F(H_2O)_2O[(O_2C)\text{-}C_6H_4\text{-}(CO_2)]_3 \cdot nH_2O(n\sim25)\}$ (MIL-101) is one of the most typical hydrogen carriers with high specific surface area, large pore volume and pore size. The structure of MIL-101 is stable and can exist in several months stably to ensure a complete structure [16]. These characteristics make MIL-101 widely used in the field of hydrogen storage [17–21]. MIL-101 has high hydrogen storage (6.1%) at liquid nitrogen temperature, but the hydrogen storage is very low (0.36%) at room temperature. Researchers have chosen MIL-101 to combine with graphene oxide and noble metal to increase the hydrogen storage capacity. However, there is not much research on palladium complex for improving hydrogen storage capacity. The relationship between structure and hydrogen storage capacity and the mechanism of ligand functional groups are not clear. The hydrogen storage performance of MOFs at room temperature and under normal pressure needs to be improved.

In this paper, MIL-101 ($Cr_3F(H_2O)_2O[(O_2C)C_6H_4(CO_2)]_3 \cdot nH_2O$,$n \approx 25$) with high porosity, specific surface area and stable structure had been prepared and used as a carrier. Noble metal Pd has stronger hydrogen storage ability than other metals (Pt, Fe et al.) due to its special electronic structure. Therefore, Pd was loaded by impregnation and reduction method on the MIL-101. A composite hydrogen storage material of Pd/MIL-101 with a stable structure and excellent hydrogen storage capacity had been obtained. The structures and hydrogen storage performance of MIL-101 and Pd/MIL-101 were investigated by X-ray diffraction (XRD) analysis, transmission electron microscope (TEM), X-ray photoelectron spectroscopy (XPS), specific surface area tests (BET) and the P-C-T. The hydrogen absorption enthalpy and the diffusion coefficient were calculated based on Fick's law of diffusion.

2. Experimental section

2.1. Preparation of MIL-101

The MIL-101 was prepared by solvothermal method. It was prepared by nine hydrated chromium nitrate and terephthalic acid by isothermal reaction at 170 °C in this experiment. Briefly, 2-methyl imidazole (0.328 g) was placed in 40 mL deionized water stirred for 5 min in the magnetic stirring at normal temperature. Then, 1.328 g terephthalic acid was added, stirred for 15 min, and 3.2 g nine water nitrate was added to the small beaker under continuous stirring for 15 min. The turbid liquid (100 mL) was maintained in the oven for 24 h at constant temperature of 170 °C. Then the liquid was separated centrifugally by 3000 r/min. After washing with absolute ethanol and DMF, the green solid obtained by centrifugation was dried in an oven at 100 °C for 15 h, and finally the green powder sample of 0.1958 g was obtained.

2.2. Preparation of Pd^{2+}/MIL-101 composites

The prepared MIL-101 samples (0.1958 g) were placed in a small crucible. Under the protection of nitrogen, the sample was calcined at 220 °C for 2 h. The sample was weighed 0.1135 g. The Pd was loaded by incipient-wetness impregnation method. Briefly, $PdCl_2$ (0.0720 g) was dissolved in deionized water (3 mL). The roasted MIL-101 was spread in a small crucible, and the $PdCl_2$ solution was uniformly distributed onto the MIL-101 completely. Then it was vacuum dried at 60 °C. The composite material of Pd^{2+}/MIL-101 was obtained.

2.3. Preparation of Pd/MIL-101 composites

The liquid phase chemical reduction was used to restore the product. The Pd^{2+}/MIL-101 was dispersed in the deionized water (4 mL). The $NaBH_4$ solution (1 wt%) was slowly added to the stirring side and got black powder precipitate. The black powder was burned for 2 h at 220 °C in a tubular furnace after filtrating, washing and drying. Then Pd/MIL-101 composites were obtained.

3. Results and discussion

3.1. Characterization of MIL-101 and Pd/MIL-101 by XRD

Fig. 1 shows the refined XRD patterns of the as-prepared MIL-101, burned MIL-101 and Pd/MIL-101. The observed almost same main diffraction peaks of all the three show that the composite products after loading Pd have not been changed, and the original framework of MIL-101 is remained well. The XRD patterns of Pd/MIL-101 did not show any diffraction peak of Pd, indicating that Pd nanoparticles were highly dispersed in the skeleton of MIL-101

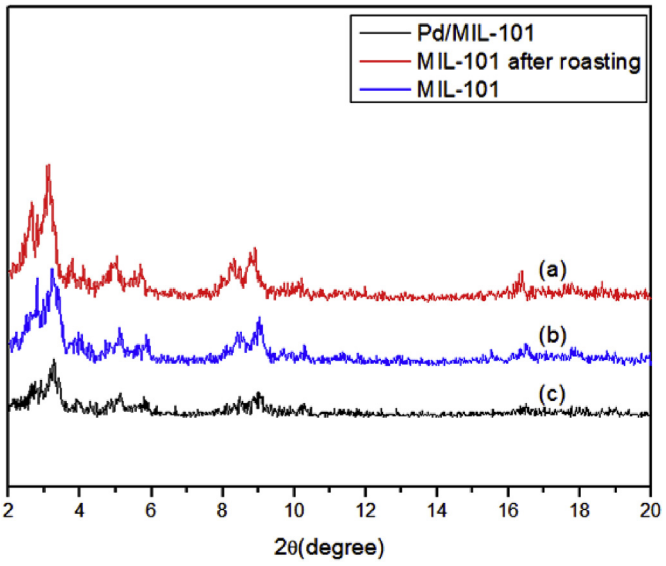

Fig. 1. Powder SEM diagrams of Pd/MIL-101 samples of (a) MIL-101; (b) burned MIL-101; and (c) Pd/MIL-101.

or its signal value was not detected because of low content of Pd (1.5%) [20–22].

3.2. Characterization of MIL-101 and Pd/MIL-101 by SEM

Fig. 2 shows the corresponding SEM images (Zeiss evo 18 electronic scanning tester) of MIL-101 and Pd/MIL-101. The size of the synthesized MIL-101 grain was uniform (Fig. 2a), the crystal exhibited eight-hedral structure of nanoscale size. Small white particles (Fig. 2b) are adhered to the eight-hedral grains of mil-101. These small white particles were Pd, which was confirmed by the EDS test in Fig. 3. It indicated that Pd was successfully loaded on the MIL-101 surface.

3.3. Characterization of Pd/MIL-101 by XPS

The valence state of Pd was tested by XPS (Escalab 250 Xi), as shown in Fig. 4. The black curve was measured, and the other color curves were simulated by peak splitting. The simulated curves were in good agreement with the measured results. Two peaks were observed at 335.18 and 340.8 eV, respectively, in the black curve. The peaks of 3d5/2 and 3d3/2 for zero valence Pd were 334.8 and 340.1 eV, respectively [23]. The peaks of 3d5/2 and 3d3/2 of Pd^{2+} were 337 and 342.3 eV [23]. From this analysis data, Pd in Pd/MIL-101 mainly existed in the reduced state, i.e., zero valence Pd [23–26].

3.4. The BET test of aperture and gaseous separation capacity of Pd/MIL-101

Fig. 5 shows the specific surface and pore structure (JW-BK122K) of MIL-101 and Pd/MIL-101, characterized with nitrogen adsorption. Compared diagrams a and b, MIL-101 loaded with Pd kept its original nature and the image was still type I adsorption isotherm (E1 ≫ En). It indicated that Pd/MIL-101 composites after Pd loading were still microporous solid. The specific surface area of Pd/MIL101 was 805.30 m^3/g, which was smaller than 1821 m^3/g of MIL-101. It was proved that the Pd nanoparticles were highly dispersed in the framework of MIL-101 and were encapsulated in the MIL-101 cage, resulting in a reduced specific surface area of the material. The pore size was 29.1 Å before loading and the pore size increased after loading. The adsorption capacity of the metal-organic frameworks was weakened with the reduction of specific surface area inevitably, which was mainly physical adsorption. However, Pd loading on the metal-organic frameworks can construct a carbon bridge between the skeletons during the synthesis of the composites with narrow pore structure. Through the potential energy overlap action of the adjacent hole wall, the force of the material and hydrogen molecules was enhanced, the binding energy of hydrogen was improved [24–27]. Therefore, the adsorption capacity of the material was greatly enhanced by chemical adsorption [27].

3.5. The analysis of Pd/MIL-101 by TEM

The Pd particles of Pd/MIL101 were characterized by TEM (FEI Tecnai G2 F20 field emission transmission electron microscopy). Pd nanoparticles (Fig. 6a–b) were evenly distributed in the channel of the carrier, with an average particle size of about 6.28 nm by measuring 150 particles, and were encapsulated in the MIL-101 hole cage without agglomeration. However, there were many Pd nanoparticles (Fig. 6c–d) with an average particle size of about 20.75 nm by measuring 125 particles, deposited on the surface of MIL-101 that were much larger than the hole cage size of MIL-101 [18–22]. This result can be verified in the results of SEM and N_2 desorption.

3.6. Thermogravimetric analysis of Pd/MIL-101

Fig. 7 shows the thermogravimetric test diagram of Pd/MIL-101. The experimental samples were tested under nitrogen protection at a heating rate of 10 °C/min from 50 to 800 °C. It can be seen that the mass loss of the sample was only 10% at 200–400 °C, and then the quality of the sample decreased rapidly. Lastly, the structure of the sample collapsed at 680 °C [24–27]. The residual mass percentage increased after 700 °C, which might be caused by the collapse of the skeleton and the side reaction of Pd at high temperature. The mass loss rate of the sample of 6.2 mg was about 35% which started to lose at 200 °C, indicating that the sample was thermally stable below 200 °C.

3.7. Test of electrochemical hydrogen storage performance

In this experiment, hydrogen diffusion coefficient was tested by electrochemical work station with a three-electrode electrochemical cell. The electrolyte used in the experiment was 6 mol/L KOH and 0.1 mol/L HCl in anode and cathode, respectively. The hydrogen diffusion coefficient (DH) can be evaluated according to Eq. (1):

$$\mathrm{Lg}(I_z - I_o) = \mathrm{Lg2}\ I_o - 0.434*(\pi/L)^2 D * t \quad (1)$$

where I_z represents the steady state diffusion current density (mA/g); I_0 is the initial diffusion current density (mA/g); D is the hydrogen-diffusion coefficient (cm^2/s); L is the thickness of the samples (mm); and t is the discharge time (s). Given Eq. (1), it is clear that the value of D can be derived from the slope of *logi–t*

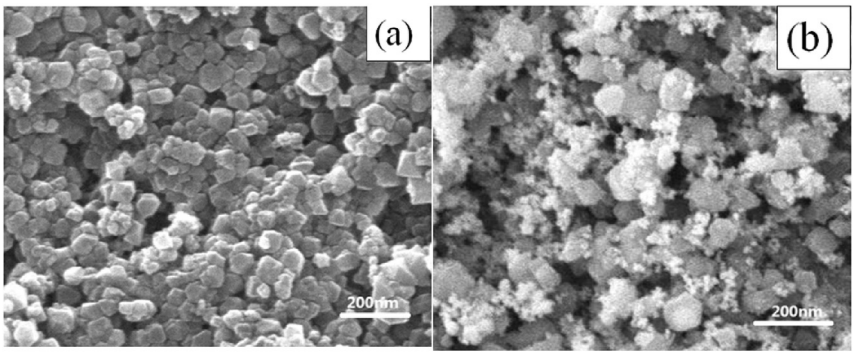

Fig. 2. SEM diagrams of (a) MIL-101; and (b) Pd/MIL-101.

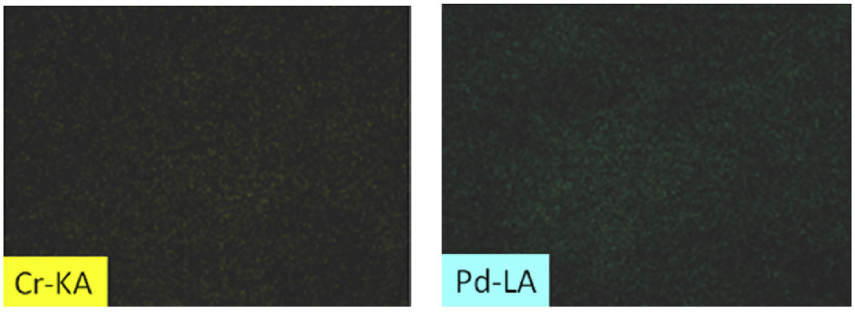

Fig. 3. EDS diagrams of Pd/MIL-101 samples.

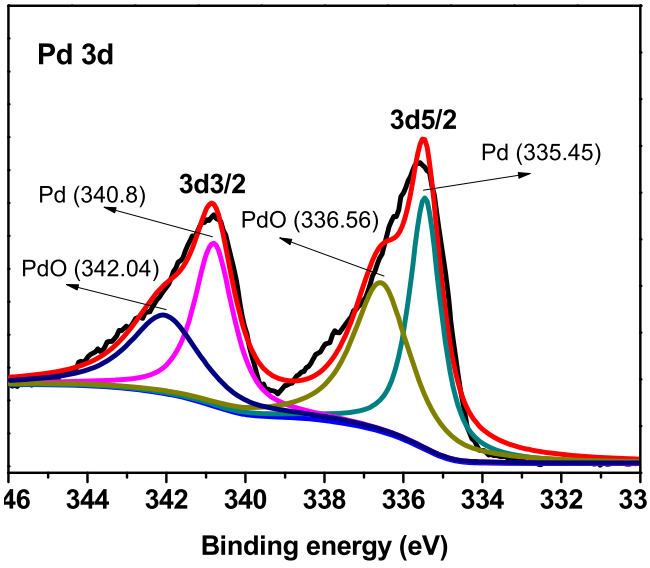

Fig. 4. XPS diagrams of Pd/MIL-101.

curves. Before testing, the alloy electrodes were prepared by mixing the alloy powders with carbonyl nickel powder at a weight ratio of 1:3 and then cold pressed into a pellet under a pressure of 10 MPa. The electrochemical studies were performed in a half-cell consisting of a working electrode, a sintered $Ni(OH)_2$/NiOOH counter electrode, and a Hg/HgO reference electrode. The electrolyte was a 6 M KOH solution.

The electrochemical test curves of MIL-101 and Pd/MIL-101 are shown in Fig. 8. The curves of steady state were fitted by $lg(I_Z\text{-}I_0)$-t. The tangent slopes of $lg(I_Z\text{-}I_0)$-t were calculated. The slope of MIL-101 material K1 was −0.005, and the slope of Pd/MIL-101 composite material K2 was −0.067. As the thickness of the samples was L1 = 0.645 mm and L2 = 0.680 mm, the results were $D_{H1} = 4.851 \times 10^{-10}$ cm/s, $D_{H2} = 7.233 \times 10^{-9}$ cm/s, calculated by the formula $k = 0.434 \times (\pi/L)^2 D$ according to Eq. (1).

It could be seen from the above calculation that the hydrogen diffusion coefficient of Pd/MIL-101 was greater than that of MIL-101, indicating that the hydrogen diffusion coefficient of the material increased after the loading of Pd. This showed that the effect of carbon bridge combination to improve the hydrogen storage capacity was more obvious by loading of Pd on MIL-101, improving the hydrogen storage capacity of the material.

3.8. PCT curves and thermodynamic parameter calculation

The pressure-composition-temperature (PCT) curves of MIL-101 and Pd/MIL-101 under 450, 500 and 550 K were determined by Sievert solid-air desorption method [29–31]. The

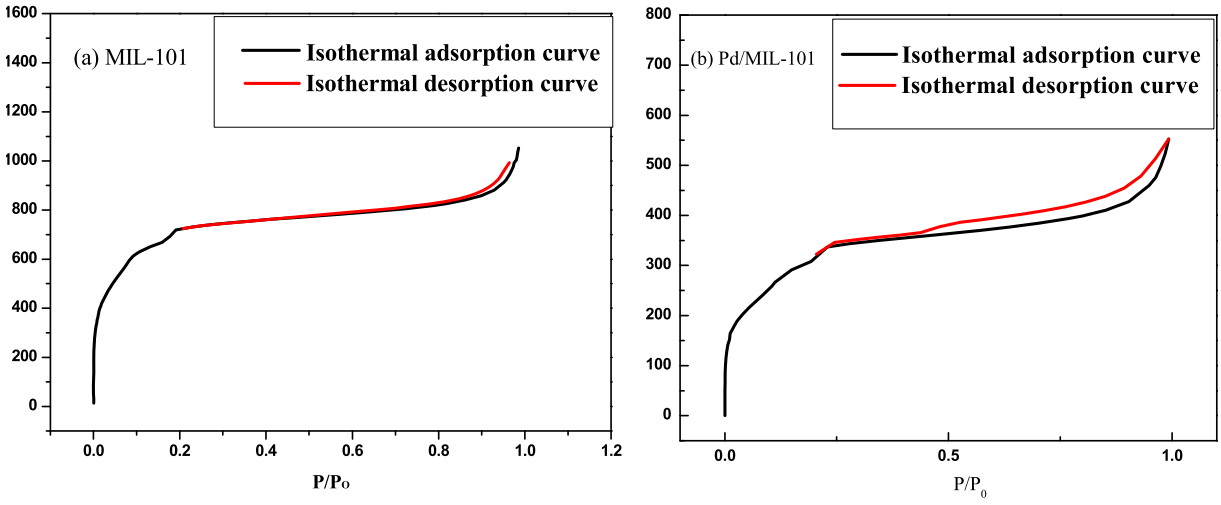

Fig. 5. Nitrogen isothermal adsorption stripping of Pd/MIL-101 and MIL-101 (25 °C).

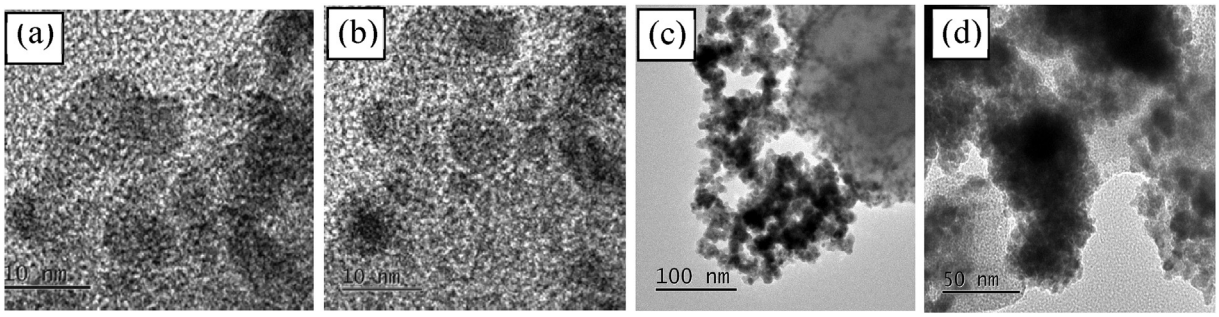

Fig. 6. (a–d) TEM diagram of Pd/MIL-101 at different location of the TEM sample grid.

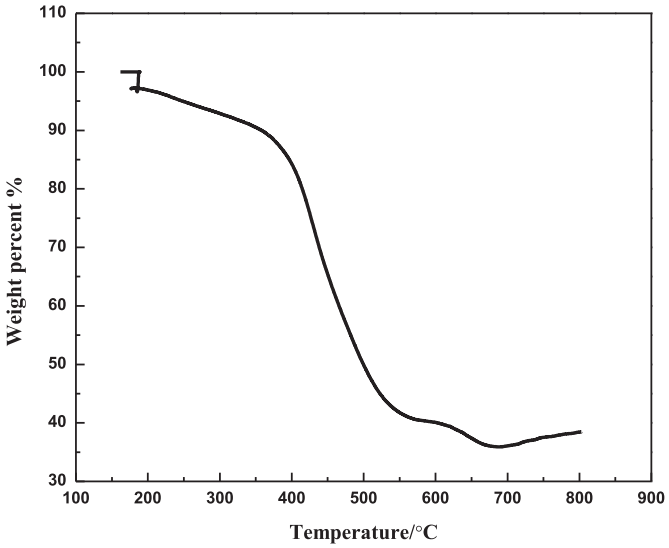

Fig. 7. Thermogravimetric curve of Pd/MIL-101.

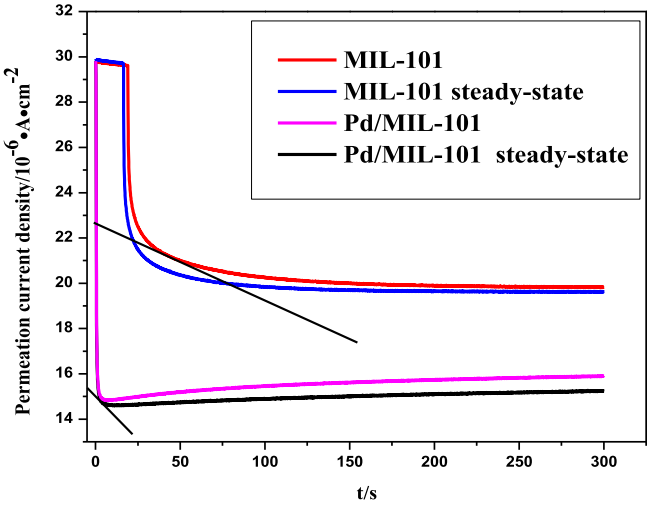

Fig. 8. Electrochemical performance test of MIL-101 and Pd/MIL-101.

representation of the Van 't Hoff equation is shown as Equation (2) [31]:

$$\ln P_{H_2} = \frac{\Delta H}{R}\cdot\frac{1}{T} - \frac{\Delta S}{R} \tag{2}$$

where P_{H2} represents the equilibrium pressure of hydrogen; ΔH is the enthalpy change of hydrogenation (kJ/mol), ΔS is the entropy change of the equilibrium system (J/mol·K); R is the molar gas constant, and T is the thermodynamic temperature (K).

From Fig. 9, it can be seen that ln (PH_2) and 1/T show a linear relationship. The enthalpy change (ΔH) of MIL-101 and Pd/MIL-101 in hydrogen absorption process can be evaluated according to Eq. (2). The R_2 values fitted by the Van 't Hoff equation were all greater than 0.999. The formation enthalpy of MIL-101 and Pd/MIL-101 is −41.59 kJ/mol and −35.24 kJ/mol, respectively. It can be seen that the enthalpy of hydrogen absorption formed after MIL-101 loaded with Pd is smaller, and the stored hydrogen is easily released because of the unstable metal hydride [32]. The equilibrium hydrogen pressure is increased, that may be caused by Pd entering the hole of the compound. As a result, the resistance of H atoms into the channel increases with some lattice distortion and strain increasing, and the stability of the hydride decreases. In addition, it is beneficial for H atoms enter and deposit skeleton compounds, resulting in a higher hydrogen storage capacity of the composites. A carbon bridge between the skeleton existing in the narrow pore structure of the composite is constructed due to the loaded Pd on the metal organic skeleton compound. By the potential energy overlap of the adjacent hole wall, the interaction between the material and hydrogen is enhanced and the hydrogen binding energy is improved. Therefore, the adsorption capacity of the material is greatly enhanced [24–30]. With so many advantages over metal, ceramic, carbon, polymers and their nanocomposites, this system can be used for other applications as well [32–60].

4. Conclusions

In this study, Pd/MIL-101 were prepared by solvothermal method and equal impregnation method. The material kept its three dimensional topology after Pd loading. The materials were microporous before and after the load of Pd. A large number of nanoscale Pd particles entered the channel and some particles adhered to the surface. The specific surface area was decreased due to the occupying of some micropores by the entered nanoscale Pd particles in the channel. The Pd/MIL-101 had a higher D_H value (7.233×10^{-9} cm/s), lower hydride-formation enthalpy ($\triangle H = -35.24$ kJ/mol) and good thermal stability. Overall, these results show that the Pd load reduced the enthalpy of hydride generation, increased the hydrogen diffusion coefficient, and

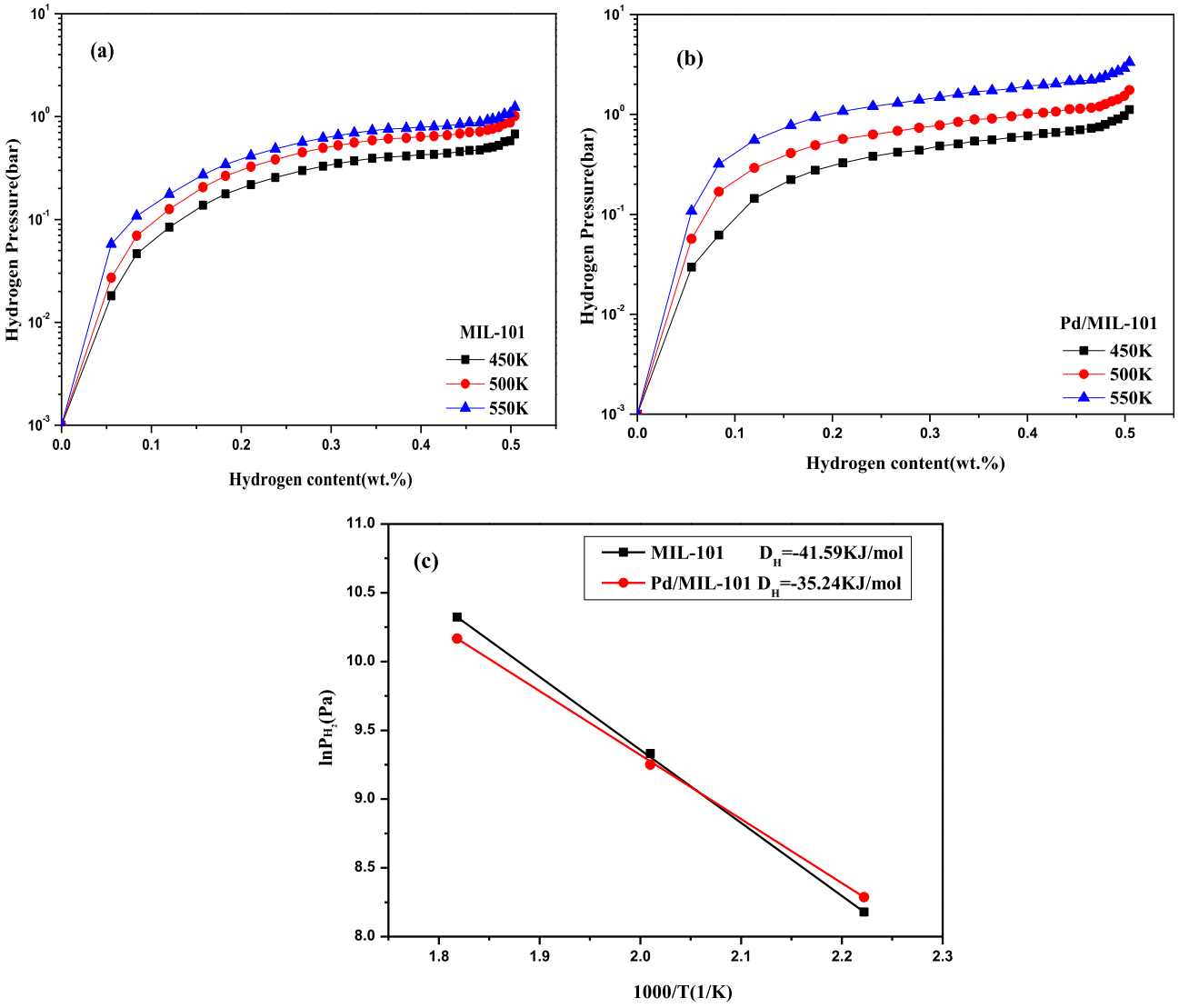

Fig. 9. PCT curves and thermodynamic enthalpy curves of MIL-101 and Pd/MIL-101.

improved the hydrogen storage capacity of MIL-101 through the potential energy overlap of the adjacent hole wall.

Acknowledgements

This work was financially supported by the National Natural Science Foundation of China (51471055), the Fund for Key supports funding projects for Discipline Construction of Shanxi province (Jinjiao research [2015]10), the Leader of the youth discipline of Taiyuan Institute of Technology, Shanxi "1331 Project" Collaborative Innovation Center, the Shanxi Province Foundation for Youths (2015021072), the Program for the Innovative Talents of Taiyuan Institute of Technology(TITXD201403), Special Youth Science and Technology Innovation (QKCZ201635), National Training Programs of Innovation and Entrepreneurship for Undergraduates (201614101004),Shanxi Province funded project for returning students(2017-109).

References

[1] O.I. Lebedev, F. Millange, C. Serre, et al., First direct imaging of giant pores of the metal-organic framework MIL-10, Chem. Mater. 17 (2005) 6525–6527.
[2] G. Ferey, C. Mellot-Draznieks, C. Serre, et al., A chromium terephthalate based solid with unusually large pore volumes and surface area, Science 309 (2005) 2040–2042.
[3] Z. Zhao, R. Guan, J. Zhang, Z. Zhao, P. Bai, Effects of process parameters of semisolid stirring on microstructure of Mg-3Sn-1Mn-3SiC (wt%) strip processed by rheo-rolling, Acta Metall. Sin. (Engl. Lett.) 30 (2017) 66–72.
[4] T. Su, Q. Shao, Z. Qin, Z. Guo, Z. Wu, Role of interfaces in two-dimensional photocatalyst for water splitting, ACS Catal. 8 (2018) 2253–2276.
[5] X. Yang, Z. Wang, L. Shao, Construction of oil-unidirectional membrane for integrated oil collection with loss less transportation and oil-in-water emulsion purification, J. Membr. Sci. 549 (2018) 67–74.
[6] H. Sun, X. Yang, Y. Zhang, et al., Segregation-induced in situ hydrophilic modification of poly (vinylidene fluoride) ultrafiltration membranes via sticky poly (ethylene glycol) blending, J. Membr. Sci. 563 (2018) 22–30.
[7] Z. Zhao, P. Bai1, R. Guan, V. Murugadoss, H. Liu, X. Wang, Z. Guo, Microstructural evolution and mechanical strengthening mechanism of Mg-3Sn-1Mn-1La alloy after heat treatments, Mater. Sci. Eng. A 734 (2018) 200–209.
[8] X. Jiang, S. Li, S. He, et al., Interface manipulation of CO_2-philic composite membranes containing designed UiO-66 derivatives towards highly efficient CO_2 capture, J. Mater. Chem. A 6 (2018) 15064–15073.
[9] N.L. Rosi, J. Echert, M. Eddaoudi, et al., Hydrogen storage inmicroporousmetal-organic frameworks, Science 300 (2003) 1127–1129.
[10] A.G. Wong-Foy, A.J. Matzger, O.M. Yaghi, Exceptional H_2 saturation uptake in microporous metal-organic frameworks, J. Am. Chem. Soc. 128 (2006) 3494–3495.
[11] J.L.C. Rowsell, A.R. Millward, K.S. Park, et al., Hydrogen sorption in functionalized metal-organic frameworks, J. Am. Chem. Soc. 126 (2004) 5666–5667.
[12] H.K. Chae, D.Y. Siberio-Pérez, J. Kim, et al., A route to high surface area,

porosity and inclusion of large molecules in crystals, Nature 427 (2004) 523–527.
[13] K.L. Mulfort, J.T. Hupp, Chemical reduction of metalorganic framework materials as a method to enhance gas uptake and binding, J. Am. Chem. Soc. 129 (2007) 9604–9605.
[14] Y. Liu, J. Zeng, J. Zhang, et al., Improved hydrogen storage in the modified metal-organic frameworks by hydrogen spillover effect, Int. J. Hydrogen Energy 32 (2007) 4005–4010.
[15] H. Du, Y. An, Y. Wei, et al., Nickel powders modified nanocoating strengthened iron plates by surface mechanical attrition alloy and heat treatment, Sci. Adv. Mater. 10 (2018) 1063–1072.
[16] L. Zhang, M. Qin, et al., Heterostructured TiO_2/WO_3 nanocomposites for photocatalytic degradation of toluene under visible light, J. Electrochem. Soc. 164 (2017) H1086–H1090.
[17] G. Ren, B. Ma, H. Liang, et al., Performance study of $Fe_2O_3/CeO_2/Al_2O_3$ oxygen Carrier in chemical looping hydrogen production, Chin. J. Rare Earths Sci. 6 (2014) 679–684.
[18] J. Zhou, Y. Zheng, J. Xie, Research progress of hydrogen production technology and its application prospect in fuel cell, J. Chem. Ind. 5 (2007) 71–75.
[19] D. Wu, X. Zhang, J. Zhu, D. Cheng, Concerted catalysis on tanghulu-like Cu@zeolitic imidazolate framework-8 (ZIF-8) nanowires with tuning catalytic performances for 4-nitrophenol reduction, Eng. Sci. 2 (2018) 49–56, https://doi.org/10.30919/es8d718.
[20] Y. Wang, P. Zhou, S. Luo, et al., Controllable synthesis of monolayer poly(-acrylic acid) on channel surface of mesoporous alumina for Pb(II) adsorption, Langmuir 34 (2018) 7859–7868.
[21] X. Zhang, H. Wang, X. Yan, X. Zhang, DFT study of hydrogen storage capacity of organic ligand BDC in MOF-5, Sci. Technol. Commun. 3 (2014) 133–134.
[22] C. Wang, M. Zhao, J. Li, et al., Silver nanoparticles/graphene oxide decorated carbon fiber synergistic reinforcement in epoxy-based composites, Polymer 131 (2017) 263–271.
[23] H. Xu, M. Zhang, X. Huang, D. Shi, Palladium nanoparticles supported on MIL-101 as an efficient heterogeneous catalyst for selective C_2 arylation of benzofuran, Chin. J. Org. Chem. 38 (2018) 832.
[24] Y. Li, R.T. Yang, Hydrogen storage in metal-organic frameworks by bridged hydrogen spillover, J. Am. Chem. Soc. 128 (2006) 8136.
[25] S. Jian, Y. Li, MIL-101 supported Ni@Pd core shell nanoparticles for hydrogenation of aromatic nitro compounds, J. Catal. 1 (2016) 91–97.
[26] J. Huang, Y. Cao, Q. Shao, et al., Magnetic nanocarbon adsorbents with enhanced hexavalent chromium removal: morphology dependence of fibrillar vs particulate structures, Ind. Eng. Chem. Res. 56 (2017) 10689–10701.
[27] Y. Liu, J. Zhang, L. Zeng, H. Zhu, et al., The hydrogen storage performance of metal-organic frameworks loaded with nickel under mild conditions, J. Catal. 07 (2008) 655–659.
[28] F. Liu, Y. Su, Z. Wang, S. Pan, Fick's law in the study of hydrogen diffusion coefficient, J. Guangxi Univ. 5 (2010) 1001–7445.
[29] Z. Xu, Z. Wang, J. Tang, et al., Effects of Mo alloying on the structure and hydrogen-permeation properties of Nb metal, J. Alloys Compd. 740 (2018) 810–815.
[30] F. Liu, Z. Xu, Z. Wang, et al., Structures and mechanical properties of Nb-Mo-Co(Ru) solid solutions for hydrogen permeation, J. Alloys Compd. 756 (2018) 26–32.
[31] Darren P. Broom, in: Y. Liu, H. Pan, M. Gao (Eds.), Hydrogen Storage Materials-the Characterization of Their Storage Properties, Machinery Industry Press, 2013, pp. 63–70, etc., translation.
[32] Z. Sun, et al., Experimental and simulation understanding of morphology controlled barium titanate nanoparticles under co-adsorption of surfactants, CrystEngComm 19 (2017) 3288–3298.
[33] L. Zhang, W. Yu, C. Han, et al., Large scaled synthesis of heterostructured electrospun TiO2/SnO2 nanofibers with an enhanced photocatalytic activity, J. Electrochem. Soc. 164 (2017) H651–H656.
[34] L. Zhang, M. Qin, W. Yu, et al., Heterostructured TiO2/WO3 nanocomposites for photocatalytic degradation of toluene under visible light, J. Electrochem. Soc. 164 (2017) H1086–H1090.
[35] Y. Zhang, L. Qian, W. Zhao, et al., Highly efficient Fe-N-C nanoparticles modified porous graphene composites for oxygen reduction reaction, J. Electrochem. Soc. 165 (2018) H510–H516.
[36] B. Song, T. Wang, H. Sun, et al., Two-step hydrothermally synthesized carbon nanodots/WO3 photocatalysts with enhanced photocatalytic performance, Dalton Trans. 46 (2017) 15769–15777.
[37] X. Lou, C. Lin, Q. Luo, et al., Crystal-structure modification enhanced $FeNb_{11}O_{29}$ anodes for lithium-ion batteries, ChemElectroChem 4 (2017) 3171–3180.
[38] C. Lin, H. Hu, C. Cheng, K. Sun, X. Guo, Q. Shao, J. Li, N. Wang, Z. Guo, Nano-$TiNb_2O_7$/carbon nanotubes composite anode for enhanced lithium-ion storage, Electrochim. Acta 260 (2018) 65–72.
[39] Q. Hou, J. Ren, H. Chen, et al., Synergistic hematite-fullerene electron extracting layers for improved efficiency and stability in perovskite solar cells, ChemElectroChem 5 (2018) 726–731.
[40] J. Tian, Q. Shao, X. Dong, et al., Bio-template synthesized NiO/C hollow microspheres with enhanced Li-ion battery electrochemical performance, Electrochim. Acta 261 (2018) 236–245.
[41] B. Zhao, Q. Shao, L. Hao, et al., Yeast-template synthesized Fe-doped cerium oxide hollow microspheres for visible photodegradation of acid orange 7, J. Colloid Interface Sci. 511 (2017) 39–47.
[42] Y. Li, T. Jing, G. Xu, et al., 3-D magnetic graphene oxide-magnetite poly(vinyl alcohol) nanocomposite substrates for immobilizing enzyme, Polymer 149 (2018) 13–22.
[43] W. Zhu, S. Ge, Q. Shao, Adsorption properties of ZrO_2 hollow microboxes prepared using $CaCO_3$ cubes as templates, RSC Adv. 6 (2016) 81736–81743.
[44] J. Zhao, L. Wu, C. Zhan, et al., Overview of polymer nanocomposites: computer simulation understanding of physical properties, Polymer 133 (2017) 272–287.
[45] X. Cui, G. Zhu, Y. Pan, et al., Polydimethylsiloxane-titania nanocomposite coating: fabrication and corrosion resistance, Polymer 138 (2018) 203–210.
[46] C. Wang, B. Mo, Z. He, et al., Hydroxide ions transportation in polynorbornene anion exchange membrane, Polymer 138 (2018) 363–368.
[47] C. Cheng, et al., Tunable and weakly negative permittivity in carbon/silicon nitride composites with different carbonizing temperatures, Carbon 125 (2017) 103–112.
[48] Z. Wu, S. Gao, L. Chen, et al., Electrically insulated epoxy nanocomposites reinforced with synergistic core-shell SiO2@MWCNTs and montmorillonite bifillers, Macromol. Chem. Phys. 218 (2017), 1700357.
[49] Y. Zheng, Y. Zheng, Z. Wang, et al., Sodium dodecyl benzene sulfonate-catalyzed reaction for aromatic aldehydes with 1-phenyl-3-methyl-5-pyrazolone in aqueous media, Green Chem. Lett. Rev. 11 (2018) 217–223.
[50] Z. Hu, D. Zhang, F. Lu, , et al.Y. Huang, Multistimuli-responsive intrinsic self-healing epoxy resin constructed by host–guest interactions, Macromolecules 51 (2018) 5294–5303.
[51] Z. Hu, Q. Shao, Y. Huang, et al., Light triggered interfacial damage self-healing of poly(p- phenylene benzobisoxazole) fiber composites, Nanotechnology 29 (2018), 185602.
[52] J. Guo, H. Song, H. Liu, et al., Polypyrrole-interface-functionalized nano-magnetite epoxy nanocomposites as electromagnetic wave absorber with enhanced flame retardancy, J. Mater. Chem. C 5 (2017) 5334–5344.
[53] Z. Wang, R. Wei, J. Gu, et al., Ultralight, highly compressible and fire-retardant graphene aerogel with self-adjustable electromagnetic wave absorption, Carbon 139 (2018) 1126–1135.
[54] N. Wu, C. Liu, D. Xu, et al., Enhanced electromagnetic wave absorption of three-dimensional porous Fe_3O_4/C composite flowers, ACS Sustain. Chem. Eng. 6 (2018) 12471–12480, https://doi.org/10.1021/acssuschemeng.8b03097.
[55] Y. Lu, M.C. Biswas, Z. Guo, J. Jeon, E.K. Wujcik, Recent developments in bio-monitoring via advanced polymer nanocomposite-based wearable strain sensors, Biosens. Bioelectron. (2018), https://doi.org/10.1016/j.bios.2018.08.037 in press.
[56] H. Liu, Y. Ding, B. Yang, Z. Liu, Q. Liu, X. Zhang, Colorimetric and ultrasensitive detection of H_2O_2 based on Au/Co_3O_4-CeO_x nanocomposites with enhanced peroxidase-like performance, Sensor. Actuator. B Chem. 271 (2018) 336–345.
[57] X. Zhu, W. Chen, K. Wu, H. Li, M. Fu, Q. Liu, X. Zhang, Colorimetric sensor of H_2O_2 based on Co_3O_4-montmorillonite nanocomposites with the peroxidase activity, New J. Chem. 42 (2018) 1501–1509.
[58] M. Chen, Y. Ding, Y. Gao, X. Zhu, P. Wang, Z. Shi, Q. Liu, N,N'-di-carboxy methyl perylene diimides (PDI) functionalized CuO nanocomposites with enhanced peroxidase-like activity and their application in visual biosensing of H_2O_2 and glucose, RSC Adv. 7 (2017) 25220–25228.
[59] Z. Hu, D. Zhang, L. Yu, Y. Huang, Light-triggered C60 release from a graphene/cyclodextrin nanoplatform for the protection of cytotoxicity induced by nitric oxide, J. Mater. Chem. B 6 (2018) 518–526.
[60] Z. Hu, C. Wang, F. Zhao, et al., Fabrication of a graphene/C60 nanohybrid via gamma-cyclodextrin host-guest chemistry for photodynamic and photothermal therapy, Nanoscale 9 (2017) 8825.